ACS OMEGA

http://pubs.acs.org/journal/acsodf

Article

Scalable Inhibitors of the Nsp3−Nsp4 Coupling in SARS-CoV-2

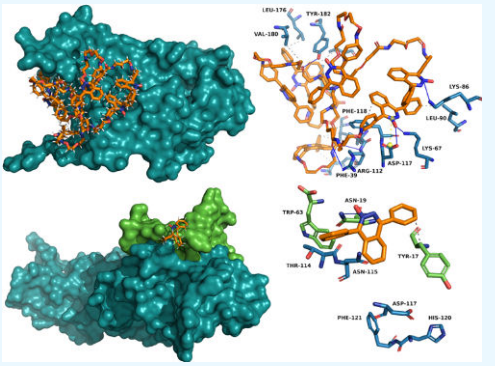
Abdul-Rahman Azizogli,◆ Varun Pai,◆ Francesco Coppola,◆ Roya Jafari, Joseph B. Dodd-o, Rohan Harish, Bhavani Balasubramanian, Jatin Kashyap, Amanda M. Acevedo-Jake,* Petr Král,* and Vivek A. Kumar*

Cite This: *ACS Omega* 2023, 8, 5349−5360

Read Online

ACCESS | Metrics & More | Article Recommendations | Supporting Information

ABSTRACT: The human Betacoronavirus SARS-CoV-2 is a novel pathogen claiming millions of lives and causing a global pandemic that has disrupted international healthcare systems, economies, and communities. The virus is fast mutating and presenting more infectious but less lethal versions. Currently, some small-molecule therapeutics have received FDA emergency use authorization for the treatment of COVID-19, including Lagevrio (molnupiravir) and Paxlovid (nirmaltrevir/ritonavir), which target the RNA-dependent RNA polymerase and the 3CLpro main protease, respectively. Proteins downstream in the viral replication process, specifically the nonstructural proteins (Nsps1−16), are potential drug targets due to their crucial functions. Of these Nsps, Nsp4 is a particularly promising drug target due to its involvement in the SARS-CoV viral replication and double-membrane vesicle formation (mediated via interaction with Nsp3). Given the degree of sequence conservation of these two Nsps across the Betacoronavirus clade, their protein−protein interactions and functions are likely to be conserved as well in SARS-CoV-2. Through AlphaFold2 and its recent advancements, protein structures were generated of Nsp3 and 4 lumenal loops of interest. Then, using a combination of molecular docking suites and an existing library of lead-like compounds, we virtually screened 7 million ligands to identify five putative ligand inhibitors of Nsp4, which could present an alternative pharmaceutical approach against SARS-CoV-2. These ligands exhibit promising lead-like properties (ideal molecular weight and log *P* profiles), maintain fixed-Nsp4-ligand complexes in molecular dynamics (MD) simulations, and tightly associate with Nsp4 via hydrophobic interactions. Additionally, alternative peptide inhibitors based on Nsp3 were designed and shown in MD simulations to provide a highly stable binding to the Nsp4 protein. Finally, these therapeutics were attached to dendrimer structures to promote their multivalent binding with Nsp4, especially its large flexible luminal loop (Nsp4LLL). The therapeutics tested in this study represent many different approaches for targeting large flexible protein structures, especially those localized to the ER. This study is the first work targeting the membrane rearrangement system of viruses and will serve as a potential avenue for treating viruses with similar replicative function.



Downloaded via UNIV OF ILLINOIS CHICAGO on February 14, 2023 at 19:25:44 (UTC).
See https://pubs.acs.org/sharingguidelines for options on how to legitimately share published articles.

INTRODUCTION

SARS-CoV-2, a newly emerged Betacoronavirus, is responsible for the ongoing pandemic of severe respiratory disease, which has infected over 500 million people globally and resulted in millions of deaths.[1−3] It is one of seven human infectious coronaviruses, including, 229E, NL63, OC43, HKU1, SARS-CoV, and MERS-CoV.[4] Its 30 kilobase genome consists of positive-sense, single-stranded RNA, which encodes 16 non-structural proteins, four structural proteins (spike, envelope, nucleocapsid, and membrane), and nine accessory proteins.[4] Significantly, the SARS-CoV-2 genome shares 79% homology to SARS-CoV.[5]

Continuously emerging SARS-CoV-2 variants challenge the reliability of recently developed vaccines (Pfizer-BioNTech, Moderna, AstraZeneca, and Johnson & Johnson) and pose an ongoing threat to international health.[6−10] The Delta and later Omicron variants were classified as variants of concern by the CDC.[10,11] However, other milder variants branched from them and, altogether, now constitute the majority of COVID-19 cases.[12−14] Despite the threat posed by the new variants, vaccination efforts remain highly effective at preventing hospitalization and death and at inducing antibody neutralization activity, particularly following the administration of a booster vaccination.[15,16] With several variants exhibiting significant mutations in the spike protein conferring increased transmissibility, it is necessary to identify conserved targets further downstream, which may be approached pharmacologically to abrogate viral replication intracellularly and limit infectious spread.[16] With this in mind, we specifically chose potential drug target interactions which are downstream in the

Received: October 3, 2022
Accepted: November 29, 2022
Published: February 6, 2023



ACS Publications

© 2023 The Authors. Published by American Chemical Society

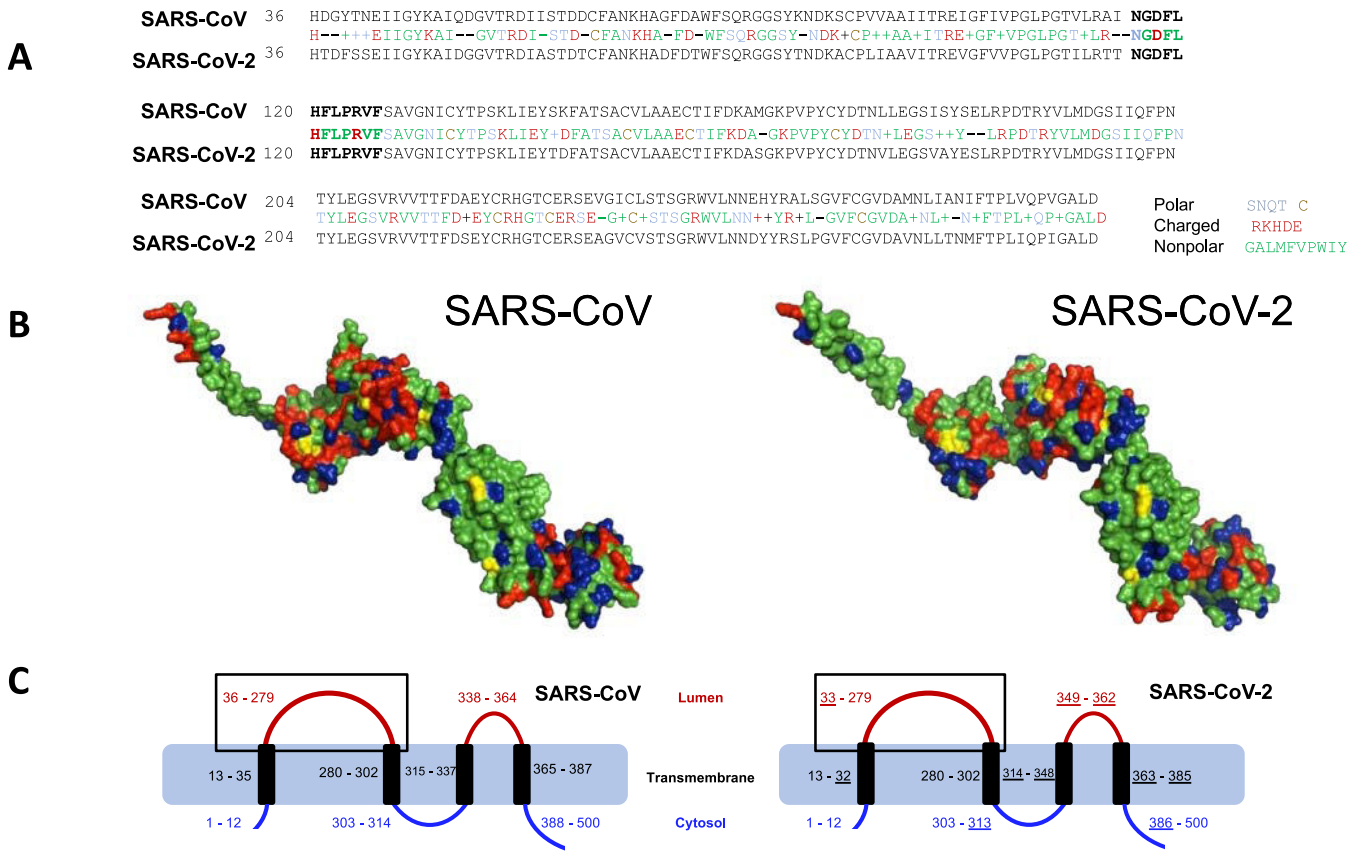


Figure 1. Overview and homology of SARS Nsp4s. (A) Sequence alignment of SARS-CoV and SARS-CoV-2 Nsp4 residues 36−279 highlighting similarities in residue type. (B) SARS-CoV Nsp4 (left) and SARS-CoV-2 Nsp4 (right) as modeled by AlphaFold2 with residues colored by type. Proteins are shown as modeled by Alphafold2 and have the potential for flexibility of transmembrane positioning due to different possible ER luminal fold orientations. (C) Transmembrane helix prediction algorithm for SARS-CoV and SARS-CoV-2 Nsp4. PBD file in Supporting Information.

viral replication process, in particular, the interaction between nonstructural protein 3 (Nsp3) and nonstructural protein 4 (Nsp4). In contrast to the Spike protein as a drug target, which is prone to antigen escape and mutation, the sequences for the relevant regions of Nsp4 and Nsp3 are well-conserved compared to SARS-CoV (about 83 and 71%, respectively), and as of this writing, Nsp4 has no identified variant mutations associated with increased virulence and transmissibility (Tables S1 and S2). Nsp4 is implicated in host membrane rearrangements to form double-membrane vesicles (DMVs), convoluted membranes (CMs), and a viral replication complex at the endoplasmic reticulum (ER) membrane; as such, it constitutes a potentially relevant target to reduce viral replication.[17,18] The Nsp4 large lumenal loop (Nsp4LLL) interacts with the C-terminus of nonstructural protein 3 (Nsp3), specifically the Nsp3 lumenal ectodomain (Nsp3Ecto); abrogation of this interaction by deletion or substitution of specific residues leads to total loss of viral replication.[18−20] In SARS-CoV-2, it has been demonstrated that Nsp3Ecto colocalizes with ER markers such as PDIA4 and coassembles with Nsp4LLL and Nsp6 lumenal loops.[21−23] Nsp3 is the central component in the formation of molecular pores with a 6-fold axis spanning DMVs and is strongly suspected to play a role in the export of viral RNA to the cytosol while avoiding a Toll-like receptor response.[24] In addition, gene ontology mapping provides strong evidence that the interaction is responsible for the disruption of endoplasmic reticulum-associated degradation (ERAD) pathways via interaction with multiple host protein partners, including DERL1, SEL1L, and RNF139.[25] Additional endogenous pathways with which Nsp3 appears to interfere include IFN-β ubiquitination, phosphorylation, RNA splicing, and NF-kB signaling, suggesting that the role of the Nsp3−Nsp4 complex is multifactorial, providing an ideal target upstream of many significant cellular aberrations involved in or affected by viral replication.[21,26,27] Although not yet clearly elucidated, Nsp3 also appears to have innate immune system-suppressing activity—specifically on the IRF-3 and (above mentioned) NF-kB pathways—across a variety of coronaviruses.[28,29]

The Nsp4 protein (Figure 1) presents a unique opportunity for targeting SARS-CoV-2 because its crucial residues have been identified, and the effect of their loss on the viral replication process has been established in the highly homologous SARS-CoV.[18] Specific Nsp4 residues identified as critical to the Nsp3−Nsp4 interaction are His[120] and Phe[121]; substitution of these residues results in the absence of CMs and viral replication bubbles within infected cells.[18] Nsp4 sequences are highly conserved among Betacoronaviruses, suggesting that potential pharmaceutical approaches targeting this protein could remain efficacious in addressing future Betacoronavirus threats, as well as against common cold coronaviruses.[18] Although not specifically targeted to Nsp4, ciclesonide—a potent inhibitor of the viral replication-transcription complex in MERS-CoV and SARS-CoV-2—was

https://doi.org/10.1021/acsomega.2c06384
ACS Omega 2023, 8, 5349−5360

identified with escape mutants bearing mutations in Nsp3 or Nsp4.[30] Interestingly, the mutation observed in Nsp4 was located at Glu^{230} in the large lumenal loop, but all of the mutations in Nsp3 which enabled ciclesonide resistance were in cytoplasmic Nsp3 domains upstream of Nsp3Ecto (and thus inaccessible to the Nsp4LLL). Clinical trials with this drug, however, did not demonstrate statistically significant improvements in patient outcomes.[30,31]

Computational drug design and virtual screening have an established record of success and have enabled the development of drugs such as oseltamivir (Tamiflu), saquinavir (Invirase), and boceprevir.[32−34] In combination with other approaches, such as molecular docking, molecular dynamics (MD) simulations with protein structures can be used to successfully identify therapeutics and targets. A typical approach relies on pre-existing structural data on target proteins and repositories containing compounds of interest. Standardized molecular docking software such as AutoDock or PyRx can be used to evaluate the binding affinity and mechanics for various compounds once a target site has been identified on the protein of interest.[35,36]

We sought to discover novel inhibitors of SARS-CoV-2 Nsp4 *in silico*, which exhibit high binding affinity to the vicinity of the His^{120} and Phe^{121} residues through a combination of virtual screening and MD simulations. In the absence of a structure validated by NMR or X-ray crystallography, protein topologies generated by deep neural network modeling provide a compelling alternative and can be used to minimize the lag time between recognition of an emergent virus and identification of potential pharmaceuticals without compromising the drug discovery process.[37−40] This approach has been validated through a comparison of experimental and predicted protein−ligand complex structures using the MEDELLER, I-TASSER, and Rosetta software.[41] More recently, AlphaFold2 has emerged as the leader in structure prediction due to its superior performance in CASP-Commons 14.[42−44] For 88% of the targets tested during this event, the AlphaFold2 predictions were accurate to within 4 Å—this number remained high at thresholds below 3 and 2 Å as well.[43] The average RMSD was recorded as 1.6 Å, close to the threshold accepted for experimental data due to slightly lower energy conformations or experimental artifacts.[45,46] In addition to this, AlphaFold modeling has been tested to agree most with the Rosetta suite in terms of stability and performs well for membrane proteins, especially for nonstructural proteins (including Nsp4) in SARS-CoV-2.[42,47] Due to AlphaFold's evolved protein modeling capabilities, highly plausible and stable Nsp4 protein structures were made in this study and serve as a reliable starting point for studying the interaction mechanisms and gauging small molecule and peptide binders. The combined approach of high throughput virtual screening and deep neural network structure prediction provides a unique method to test databases of existing compounds and to reduce the total cost of drug development studies. Furthermore, homology of function and structure can be established via protein−protein docking and protein−protein interaction analysis.

For our study, molecules with high log *P* values according to the ZINC database were prioritized for the virtual screen, given that increased lipophilicity leads to increased transmissibility through biological membranes.[48] Higher log *P* values are additionally associated with a greater capacity to form drug suspensions, which are more suitable for pharmaceutical applications and nanoparticle drug delivery into lung epithelial cells when used with the appropriate delivery device, such as perfluorocarbons.[49] The log *P* filter is an effective approach for improved local bioavailability in the tissues and cell types most affected by SARS-CoV-2 due to specific expression of the ACE2 and TMPRSS2 membrane proteins in lung and renal tissue.[50,51] There is also evidence that greater hydrophobic character contributes to elevated airway absorption. Determining suitable ligands is a complex process, however, which has previously been operationalized by multiple algorithms.[52−55] While the widely-cited rule of five developed by Lipinski has undergone subsequent modifications, we limited the compounds to a specific range of log *P* and molecular weight (MW) values using this algorithm as a preliminary filter.[55] After identifying molecules with suitable properties and high binding affinity to the Nsp4 lumenal loop region, we found the interacting residues that bind the drugs in static docking conditions. The protein−ligand binding affinity and RMSD were then calculated using atomistic molecular dynamics (MD) simulations with fixed Nsp4LLL backbone conditions. Multimeric dendrimer binders and Nsp3-derived peptides were designed to increase stability, Nsp4 binding, and inhibition akin to our previous strategies.[56] MD simulations of these constructs highlight the improvement in binding affinity and stability for drug inhibition and are attractive alternatives for inhibiting a critical step of coronavirus replication and infection.

RESULTS

The amino acid sequence of Nsp3 in SARS-CoV exhibits 75.82% identity to its corresponding sequence in SARS-CoV-2 (NP_828862.2). A comparison of Nsp4 homologous sequences in SARS-CoV and SARS-CoV-2 yielded an 80% sequence identity (Table S1). In SARS-CoV, the Nsp3Ecto is located between residues 1414−1495 on Nsp3, and residues 36−279 on Nsp4 constitute the Nsp4LLL.[18,19] The SARS-CoV Nsp3Ecto domain shows 70.73% homology with the corresponding region of SARS-CoV-2 Nsp3 (residues 1437−1518), indicating the potentially conserved role of the Nsp3−Nsp4 interaction in viral function. Of the 40 amino acids in the SARS-CoV Nsp3Ecto that are hydrophobic, 37 of the corresponding positions in SARS-CoV-2 Nsp3 have either the same amino acid or a similar hydrophobic amino acid, representing 92.5% sequence similarity. Of the entire Nsp3Ecto domain, there is only a 1.2% difference in the number of hydrophobic amino acids. This information suggests that the hydrophobic properties of the SARS-CoV Nsp3Ecto are conserved in SARS-CoV-2, and that the Nsp4-Nsp3 interaction likely would proceed by a similar biochemical mechanism. There is also some degree of conservation when compared with the other coronaviruses MERS-CoV, 229E, NL63, OC43, and HKU1, suggesting that these may also be susceptible to similar targeting (Table S1).

The SARS-CoV Nsp4LLL aligns with residues 36−279 in SARS-CoV-2 Nsp4 and exhibits 82.79% sequence identity (Figure 1A). Additionally, of the 123 hydrophobic residues in the SARS-CoV Nsp4LLL, 114 of the corresponding positions in SARS-CoV-2 Nsp4LLL have either the same amino acid or equivalent hydrophobic amino acid, constituting 92.7% sequence similarity (Figure 1A). A comparison of the entire Nsp4LLL between the two SARS-CoV viruses demonstrates only a 1.64% difference in the total number of hydrophobic amino acids. These data suggest that the hydrophobic properties are conserved in the Nsp4LLLs between the

https://doi.org/10.1021/acsomega.2c06384
ACS Omega 2023, 8, 5349−5360

SARS coronaviruses, suggesting a similar localization within the cell and a similar chemistry of the Nsp4-Nsp3 interaction. Further support arises from the TMHMM results, which assigned residues 33−279 to the LLL in SARS-CoV-2 Nsp4, very similar to residues 36−279 which constitute the LLL in SARS-CoV (Figure 1C). As for Nsp3, the ectodomain in SARS-CoV-2 includes residues 1436−1499, while in SARS-CoV, the ectodomain consists of residues 1414−1495.

The Nsp4 models generated by AlphaFold2 for the two viruses are consistent in topology, with a template modeling score (TM-Align) of 0.7585, with the SARS-CoV-2 Nsp4 structure used as a template. The Nsp4LLLs of both viruses make up a significant portion of Nsp4 (Figure 1B) and conserved residues 115−126 form a β-sheet in each coronavirus. Conversely, the Nsp3 models are inconsistent and have a TM-Align of 0.1729. Nevertheless, protein−protein docking suggests that the interaction between the Nsp3Ecto and the Nsp4LLL may still be conserved in SARS-CoV-2, with alanine scanning results comparable to outputs of the homologous interaction in SARS-CoV (Figure 2). ClusPro

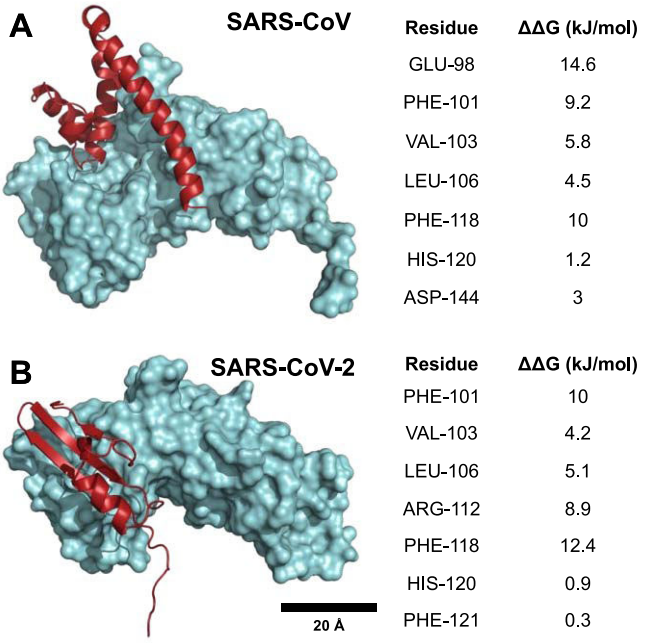


Figure 2. Docking of Nsp3Ecto and Nsp4LLL. Molecular docking was done on SARS-CoV (A) and SARS-CoV-2 (B) via ClusPro, and top complexes are shown. Alanine scanning was done by BAlaS, and the most significant ΔΔ*G*s are shown. Nsp3Ecto is shown in red, and Nsp4LLL is shown in blue.

docking scores reveal that the top clusters have comparable scores, with −1179.9 for SARS-CoV and −938.7 for SARS-CoV-2. These scores suggest strong interactions between the lumenal domains of Nsp3 and Nsp4 in both viruses and compare well to our baseline ACE2-RBD (PDB ID: 6M0J) simulation, which outputted a score equaling −1058.6.[57] The free energies of binding according to BalaS equal to ΔG = −246.25 and −155.58 kJ/mol for SARS-CoV and SARS-CoV-2, respectively. BAlaS Alanine Scanning of the docked structures highlights that the same residues play a significant role in the Nsp3−Nsp4 contact interface in both coronaviruses. Phe^{118}, Leu^{106}, Val^{103}, and Phe^{101} in Nsp4LLL show high ΔΔ*G* values in both coronaviruses and to a similar degree as well. In particular, ΔΔ*G* ∼10 kJ/mol for Phe^{118} and ∼5 kJ/mol for Leu^{106} in each virus (Figure 2). Conserved hydrophobic residues are largely responsible for this interaction, which reinforces the significance of the high conservation of hydrophobic residues between coronaviruses (Figure 1A). In addition to these largely hydrophobic residues, several charged residues such as Glu^{98} and Arg^{112} contribute to the strong interactions indicated *in silico* as well.

Following the AutoDock Vina virtual screening of the putative Nsp4 binding site, we identified five potential ligand inhibitors with high log *P* values and high binding affinity energies: ZINC116661612 (Ligand 1), ZINC4035881 (Ligand 2), ZINC19877576 (Ligand 3), ZINC5401095 (Ligand 4), and ZINC1043754 (Ligand 5), all of which occupy the putative binding pocket (Figure 3) and have significant structural and electrostatic similarity (Figure 4A−E). Each ligand is polyaromatic and contains at least one heteroatom, specifically nitrogen and/or oxygen. The similarities of the five ligands that we have identified are reflected in similar binding affinities *in silico* (Figure 4C) and in the distinctly nonpolar nature of each ligand, which gives rise to the high predicted number of hydrophobic interactions (Figure 4E). These binding affinity results lie within the energy range observed *in silico* for pharmaceuticals currently in use, such as Gleevec in complex with AbI kinase (−10.8 kcal/mol) and aspirin with Cox-1 and Cox-2 (−3.5 and −3.8 kcal/mol, respectively).[58,59] Binding affinity energies obtained *in silico* demonstrate a strong correlation with experimentally obtained values, providing an estimate of the strength of a potential Nsp4 binding drug.[60] Despite the presence of both hydrophobic interactions and hydrogen bonds, the consistently high log *P* (Figure 4D) suggests that the hydrocarbon backbone and hydrophobicity are critical in the design of binders for this pocket.

A comparison of the electrostatic charge maps suggests that there are conserved yet discrete regions of nonzero and neutral charge localized to the heteroatoms and aromatic hydrocarbon rings, respectively (Figure 4B). Although the ligands bear slight charges in their heterocyclic regions, the hydrophobic regions are the most important moieties for the strong, noncovalent interactions observed in the most stable protein−ligand complex (Figure 3). Nsp4LLL residues with nonpolar side chains such as Leu^{90}, Phe^{101}, Val^{103}, Leu^{106}, Ile^{110}, and Phe^{118} are involved in these interactions and contribute to the distinctly hydrophobic character of the interior of the cavity. The only significant residue with a charged R group is Lys^{67}, which is responsible for the formation of hydrogen bonds in Ligands 2, 4, and 5 (Figure 4E). The number and similarity of the interactions predicted suggest that the interior of the binding pocket as well as any ligand binders must be hydrophobic in nature, with any negatively charged oxygen atoms directed away from the interior residues (Figure 4). Electrostatic maps of the binding pocket further solidify the importance of nonpolar interactions as most of the contact surface has a neutral charge (Figure S1). The single distinctly positive region within the protein's binding cavity can be attributed to positively charged Lys,[67] and it interacts with highly electronegative moieties in some of the ligands (Figures S14 and 4). The residues significant to Nsp3 binding, as stated earlier, are also significant for ligand binding. Phe^{118}, Leu^{106}, Val^{103}, Phe^{101}, and Lys^{67} in Nsp4LLL are responsible for Nsp3Ecto binding and ligand binding, suggesting that the Nsp3−Nsp4 interaction can be inhibited if these ligands can sterically hinder access to biologically important residues

https://doi.org/10.1021/acsomega.2c06384
ACS Omega 2023, 8, 5349−5360

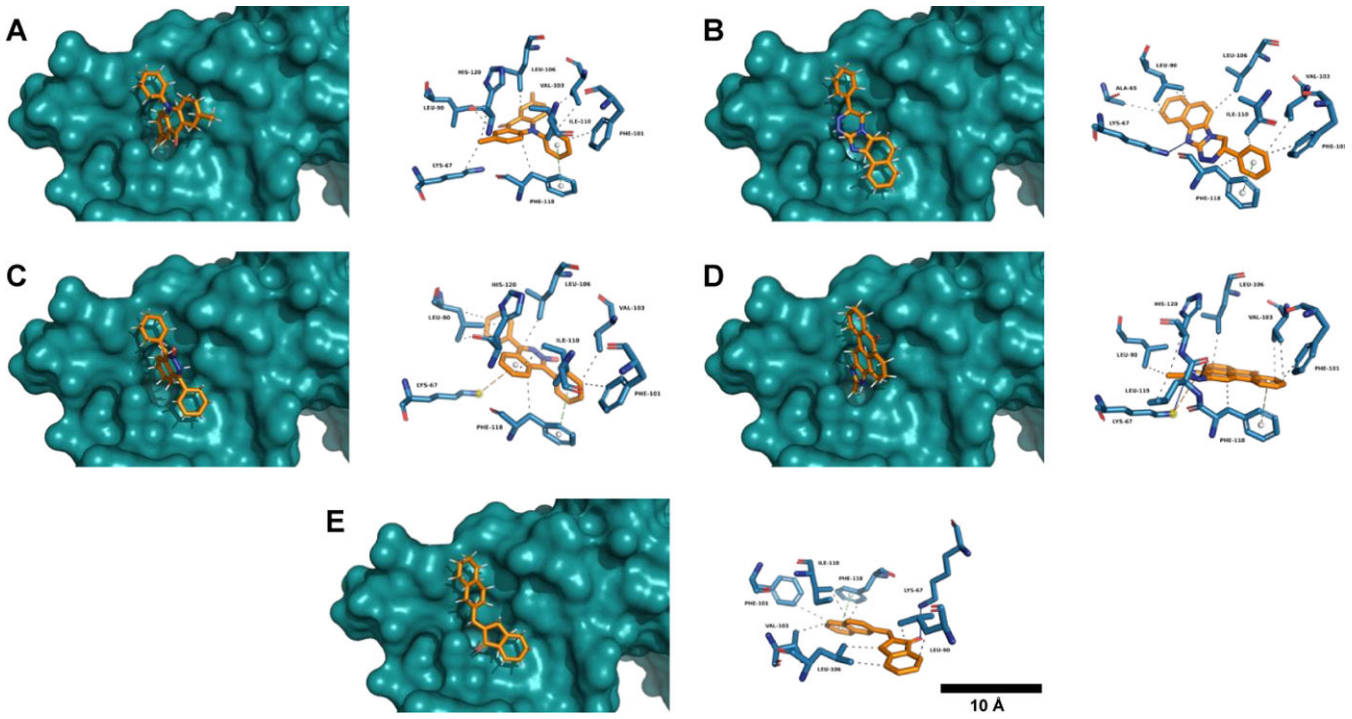


Figure 3. Protein−ligand interactions post AutoDock Vina screening. Top five small-molecule inhibitors of SARS-CoV-2 Nsp4 drug screening are shown in panels (A−E) with protein−ligand interaction profiler (PLIP) depictions of interactions on the right. Gray dashed lines show hydrophobic interactions. Solid blue lines show hydrogen bonding. Orange dashed lines show π−cation interactions, and green dashed lines show π-stacking.

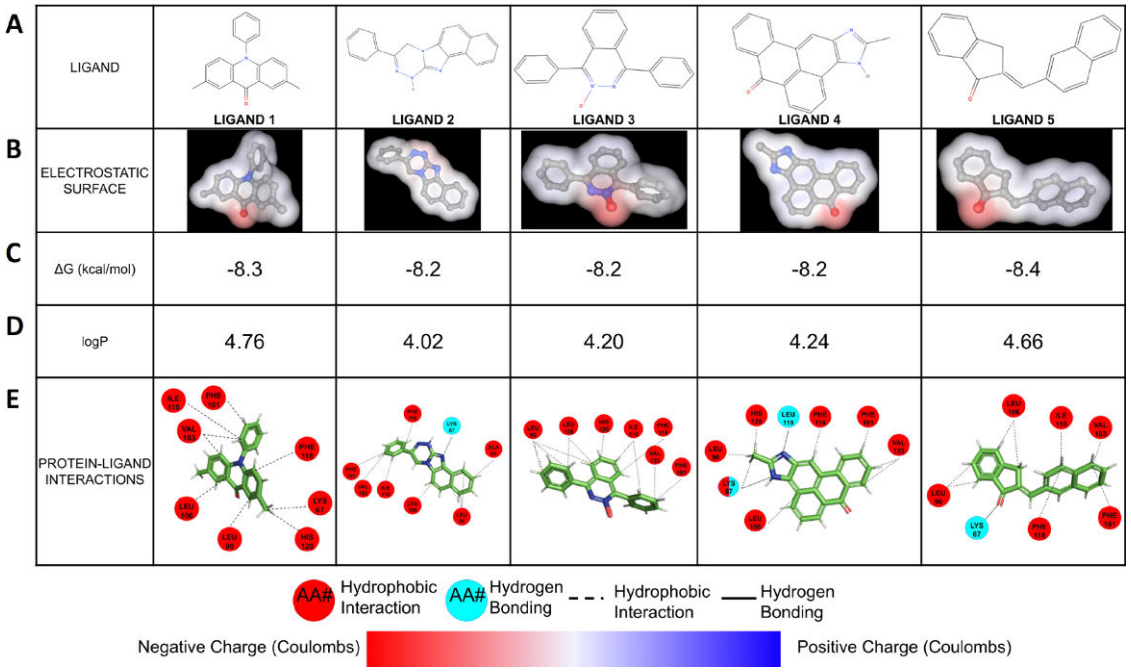


Figure 4. Overview of top five ligands. (A) Structures of the top five ligands identified based on AutoDock Vina scoring output. (B) Electrostatic charge maps of ligands generated using ESP-DNN. (C) Binding affinity energies (kcal/mol) as calculated by AutoDock Vina. (D) log P of each ligand. (E) Protein−ligand interaction profiles of each ligand on the SARS-CoV-2 Nsp4 binding pocket.

His^{120} and Phe^{121} (Figures 2 and 3). The protein−ligand interaction profiler (PLIP) results indicate identically—the ligands we have examined closely approximate the contours of the cavity (within 3−4 Å).

Simulations performed with the Nsp4LLL in complex with Nsp3Ecto suggest that the Nsp3Ecto maintains high binding affinity over time while fluctuations remain under 5 Å average RMSD (Figure S2). Subsequent simulations with the therapeutics confirmed that drugs obtained from AutoDock Vina give varying RMSDs and binding energies, with drug 1 moving the least and drug 4 moving the most from the starting position (Figure S3). Drug 3 was determined to be the best

https://doi.org/10.1021/acsomega.2c06384
ACS Omega 2023, 8, 5349−5360

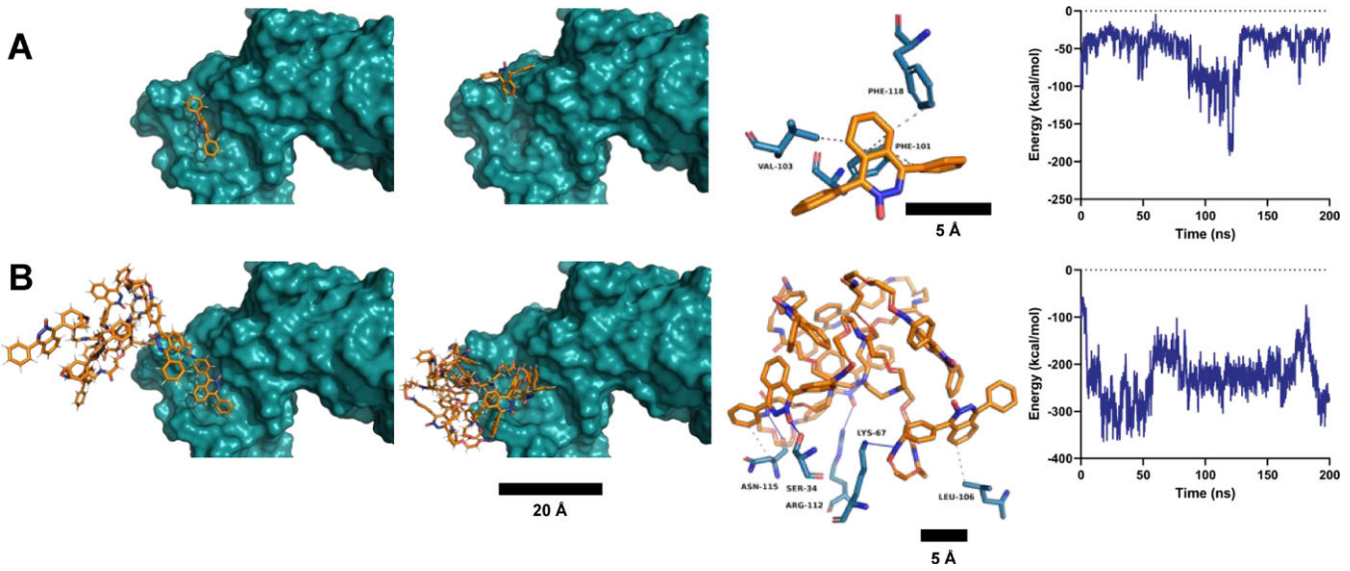
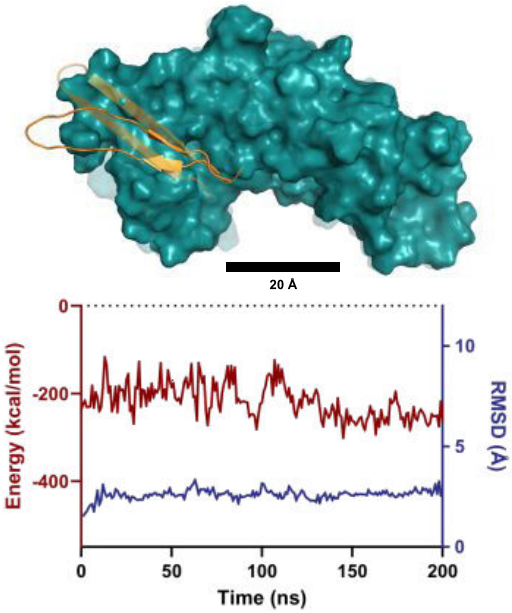


Figure 5. Drug 3 interactions in NAMD simulations. Initial (left) and final (right) simulation states of drug 3 are shown. (A) Drug 3 on SARS-CoV-2 Nsp4 simulation resulted in an average binding energy and RMSD of −52.62 kcal/mol and 1.17 Å, respectively. (B) Dendrimer with six copies of drug 3 covalently attached in complex with SARS-CoV-2 Nsp4 simulation averaged −227.24 kcal/mol and 10.45 Å. Drug Interactions are shown with protein−ligand interaction profiler (PLIP) on the right of the final PDB file. Gray dashed lines show hydrophobic interactions. Solid blue lines show hydrogen bonding. Orange dashed lines show π−cation interactions, and green dashed lines show π−stacking. The blue molecule is Nsp4, and orange is the ligand.



Peptide Residue	ΔΔG (kJ/mol)	Nsp4 Residue	ΔΔG (kJ/mol)
THR-11	1.0	MET-33	4.0
TYR-13	8.9	LYS-67	4.5
GLU-15	7.1	LYS-86	5.0
TYR-17	2.1	LEU-90	3.7
ASN-22	6.6	LEU-106	3.9
THR-24	4.0	ARG-112	2.4
TYR-28	5.4	PHE-118	6.2

Peptide Residue	ΔΔG (kJ/mol)	Nsp4 Residue	ΔΔG (kJ/mol)
THR-11	3.1	ASP-50	4.7
TYR-13	20.2	LYS-67	5.1
GLU-15	6.6	ASP-85	1.3
TYR-17	4.5	LYS-86	2.7
ASN-22	0.2	LEU-90	5.9
THR-24	1.3	LEU-106	2.4
TYR-28	11.8	PHE-118	5.7

Figure 6. Peptide inhibitor significant residues before and after NAMD simulations. Initial (transparent) and final (opaque) simulation states of peptide derived from SARS-CoV-2 Nsp3 are shown. Alanine scanning was done by BAlaS, and most significant $\Delta\Delta G$s are shown from both peptide and Nsp4 before simulation (top) and after simulation (bottom). The average binding energy and RMSD over the 200 ns simulation were −201.89 kcal/mol and 2.53 Å, respectively. Orange is the peptide, and blue is the Nsp4 protein.

drug binder with low average RMSD fluctuations of 1.17 Å and the highest absolute average binding energy of −52.62 kcal/mol (Figure S3 and Table S3). A comparison of the initial and final states of the drug 3-Nsp4LLL complex suggests that the drugs explore a lot of the Nsp4LLL protein surface and retain hydrophobic interaction with crucial phenylalanine and valine residues (Figure 5A).

As the simulations show small drugs' potential in inhibiting larger ER membrane proteins, we examined larger therapeutics such as a β hairpin extracted from the Nsp3Ecto protein and a drug-dendrimer system (Figures 6 and 5B). The branched, highly flexible dendrimer was highly efficacious, with sustained binding energies greater than −200 kcal/mol (Figure S4). From the initial to final state, the dendrimer was able to flexibly fold around the Nsp4LLL protein, forming hydrophobic interactions with the six units of drug 3 and hydrogen bonds with the drug heteroatoms and dendrimer backbone (Figure 5B). Longer simulations of 800 ns showed comparative stability of the dendrimer-Nsp4 complex after 450 ns, indicating that there is stable binding after an initial

https://doi.org/10.1021/acsomega.2c06384
ACS Omega 2023, 8, 5349−5360

exploration of the Nsp4 surface (Figure S6). The β hairpin, on the other hand, is a flat, extended peptide that can similarly adjust its structure to match changes in the binding site of Nsp4LLL and show a suitable binding energy of ∼2.5 Å, with high binding energy of ∼−200 kcal/mol (Figure S4). BUDE Alanine scanning results of initial and final simulation states suggest that mainly hydrophobic residues are implicated in the peptide−Nsp4LLL interaction as Phe[118] and Leu[106] remain significant (Figure 6). A longer 800 ns simulation of the β hairpin demonstrates that it more extensively explores the binding pocket but remains stably bound at around −200 kcal/mol (Figure S7).

Application of both the dendrimer and β hairpin in tandem through a conjugate yielded an average RMSD value of 15.72 Å and binding energy of −141.53 kcal/mol over time against the averaged value of −201.89 kcal/mol for the single peptide, showing that the dendrimer impedes the peptide from binding to the desired residues (Figure S4 and Table S3). This may be attributable to the fact that the dendrimer is carrying five other β hairpins, which are relatively large molecules with significant steric constraints. Applying β hairpins in isolation enabled them to move freely, but when bound to the dendrimer, they were large enough to pull the whole assembly (dendrimer and six β hairpins) back from the binding site.

DISCUSSION

As reported previously, the Nsp3−Nsp4 interaction is an attractive drug target due to its potential role in modulating viral replication and RNA polymerization in the absence of the critical His[120] and Phe[121] residues, underlined by the conservation of this sequence and adjacent residues in multiple members of the Betacoronaviridae family.[18] Although most applicable to pandemic viruses such as SARS-CoV, MERS-CoV, and SARS-CoV-2, pharmaceutical approaches targeting this interaction may remain appropriate for common cold viruses such as HKU1, OC43, NL63, and 229E and for newly emerged SARS-CoV-2 variants (Tables S1 and S2). Without targeting surface glycoproteins which are notorious for their rapid divergence from the original wild-type due to selective pressures, an approach aimed at abrogating the formation of the viral replication complex could provide a rapid response to future coronavirus outbreaks of epidemic or pandemic proportions.[61,62]

The presence and importance of our target have been validated *in vitro* in SARS-CoV, and the high sequence identity, when compared to SARS-CoV-2, provides additional compelling evidence to support further study on this interaction as a drug target.[18,63,64] Despite differences in the conformations and topologies of the SARS-CoV and SARS-CoV-2 Nsp3 structures and resulting Nsp3−Nsp4 complexes, many residues were identified as significant interacting residues in both viruses. Furthermore, these residues were also implicated in the PLIP analysis of the protein−ligand complexes, suggesting that a ligand that interacts with them may present a viable pharmaceutical approach if the mechanism of the interaction is conserved across Betacoronaviruses. For ligands protruding into the pocket, accessibility to His[120] and Phe[121] is hindered, and the Nsp3−Nsp4 interaction is limited.

Although our identification of ligands relied on a model of SARS-CoV-2 Nsp4, AlphaFold2 software recently tested and released to the public has demonstrated significantly higher accuracy than previously used *ab initio* modeling suites, citing a median backbone accuracy of 0.96 Å RMSD.[43] In addition to this, the protein properties we identified as significant to the ligand binding nevertheless remain pertinent for Nsp3 binding and between coronaviruses, particularly for the local residues surrounding His[120] and Phe[121]. To validate the exact mechanisms of action and other crucial residues involved in these interactions, further X-ray crystallography, cryo-EM, or NMR studies should be performed in the future. Isolating membrane proteins for these studies remains difficult, but AlphaFold2 solves the problem of protein prediction and allows for robust, accurate drug design and discovery. An examination of the ligands and the properties of the protein−protein interaction suggests that ideal inhibitory compounds will have high hydrophobicity and log P values.

The high log P values of the ZINC data set alluded to earlier in this study suggest several drug delivery modes that can be tailored to target the affected organs. Larger log P values are associated with greater rates of transport (in part due to passive transport) through the respiratory bronchial epithelium in particular and are not subject to the same transporter saturation effects associated with other drugs.[65] Other tissues such as the heart and kidneys could be targeted by similar approaches: specifically, nanoliposomes have demonstrated promise as a means by which to increase prolonged exposure of affected tissues to a drug via receptor-mediated endocytosis and to do so with greater efficacy and customization for a given drug relative to other methods.[66]

Molecular docking allowed us to identify five possible ligands for Nsp4. The MD analyses suggest fluctuation in ligand position with maintained binding energy over time for single molecules, leading to the molecules exploring the entire surface of the protein. More promising results are obtained with the use of the dendrimers or peptides as inhibitors, primarily due to the capacity of these approaches to cover more of the binding pocket and to maintain prolonged binding to the hydrophobic residues of the target Nsp4LLL. All three methods suggest different approaches for targeting a common viral mechanism localized to the ER. Initial next steps will probe antiviral efficacy, *in vitro* cytocompatibility, mutagenicity (of potential polyaromatic compounds such as those in Figure 4), and *in vivo* safety/efficacy. Further work must be done to determine suitable modes of delivery for these therapeutics and to characterize their efficacy in models of coronavirus disease.

CONCLUSIONS

This work identifies several putative and *de novo* ligands, which could be used to inhibit replication of SARS-CoV-2 within cells and reduce total viral load, ongoing challenges in the coronavirus pandemic, and arising variants. Due to the urgent need for effective pharmaceuticals, the use of neural network-mediated protein modeling (in the absence of experimentally determined X-ray or NMR structures) for drug discovery removes a major roadblock for rapid response to pandemics such as the current one. The ligands demonstrate high (absolute) binding affinity energy, exhibit deviations localized to the Nsp3Ecto binding area, and showcase promising interaction profiles both in static and dynamic simulations. Our approach targets the protein−protein interaction between the highly conserved nonstructural proteins Nsp3 and Nsp4, which could present an alternative to traditional approaches mainly targeting the main protease, RNA-dependent RNA polymerase, or spike protein. In addition, targeting a highly conserved interaction has the benefit of enabling a rapid and

https://doi.org/10.1021/acsomega.2c06384
ACS Omega 2023, 8, 5349−5360

generalized response to future coronavirus pandemics or even particularly virulent strains of common cold coronaviruses.

MATERIALS AND METHODS

Protein Sequence Homology and Structures. Protein sequences for SARS-CoV-2 Nsp3 (reference sequence: YP_009742610.1) and Nsp4 (YP_009742611.1) were obtained from the NCBI protein database. Using protein BLAST (BLASTp), homology was evaluated between the amino acid sequences of Nsp3 and Nsp4 in SARS-CoV and SARS-CoV-2 to confirm that the abrogation effect documented in the literature could potentially be conserved due to the presence of the relevant residues.[67] The identification of the SARS-CoV Nsp3Ecto domain and the SARS-CoV Nsp4LLL domain implicated in the Nsp3−Nsp4 interaction were obtained by cross-referencing with the relevant literature.[18,20] BLASTp searches were performed on these domains in SARS-CoV to determine regions of homology in SARS-CoV-2. To identify the percentage of sequence identity with the OC43, HKU1, NL63, 229E, and MERS-CoV Betacoronaviruses, BLASTp was carried out with the SARS-CoV-2 Nsp3 and Nsp4 sequences, both in totality as well as restricted to the ectodomain and large lumenal loop, respectively (Table S2). Due to the absence of validated SARS-CoV and SARS-CoV-2 structures, 3D structures generated by deep neural network analysis using AlphaFold2 were used.[43,44] The complete predicted structure for SARS-CoV-2 Nsp4 had already been prepared by AlphaFold faculty.[68] The Nsp3Ecto for both viruses and the whole SARS-CoV Nsp4 were also generated via AlphaFold. On SARS-CoV-2, the examined Nsp3Ecto domain consisted of residues 1436−1499, and the Nsp4LLL consisted of residues 33−279, as obtained from BLASTp results. SARS-CoV Nsp3Ecto and Nsp4LLL were trimmed to residues 1414−1495 and 36−279, respectively (Figure 1C). Sequence comparisons between these domains on SARS and SARS-CoV-2 was performed to determine the total homology of the region, particularly with respect to hydrophobic residues and their significance in protein−protein interactions involving membrane-bound proteins.[69]

Transmembrane Helix Prediction. To identify similarities in the Nsp4 amino acid sequences constituting lumenal loops, transmembrane helices, and cytosolic regions, various transmembrane helix prediction algorithms were tested using the Constrained Consensus TOPology (CCTOP) prediction server.[70] The TMHMM algorithm was established as the most accurate (100% of the amino acids were assigned to the correct region), and the SARS-CoV-2 sequence was subsequently tested for Nsp3 and Nsp4.

Protein−Protein Docking and Alanine Scanning. To assess the interaction between Nsp3 and Nsp4 in SARS-CoV-2, protein−protein docking of the implicated luminal loop and ectodomain residues was performed on ClusPro, a rigid body docking server that uses an energy minimization algorithm to refine, score, and cluster docked protein complexes.[71] Due to its cluster-based scoring algorithm, the center ClusPro score of the docked models was used. PDB structures for Nsp3Ecto and Nsp4LLL were submitted to ClusPro for SARS-CoV and SARS-CoV-2 to assess the total sequence conservation and similarity of the interaction between coronaviruses and to visualize the protein interactions. To gain additional insight into the specific interactions occurring at the protein−protein interface, the BAlaS BUDE Alanine scanning algorithm was used to calculate $\Delta\Delta G$ values for substitutions of each residue with Ala.[72]

Ligand Database. Ligands for testing were obtained from the ZINC compound database.[73] We filtered our initial ligand data set using ZINC's Tranche tool and limited the search to 7 million lead-like compounds with ideal log P (1−5) and molecular weight (0−400 Da) values in accordance with the rule of five.[55] The data sets were processed using Open Babel to convert them from SDF format into PDBQT format, which made the ligand files compatible with AutoDock Vina.[74,75] Ligand files were prepared by adding polar hydrogens with AutoDockTools.

Molecular Docking and Virtual Screening Process. Molecular docking simulations were carried out with the ligands and the entire SARS-CoV-2 Nsp4 using AutoDock Vina.[75] Grid dimensions were manually localized near the residues of interest (His^{120} and Phe^{121}) for SARS-CoV-2 Nsp4, and all necessary predocking modifications were carried out using the AutoDockTools GUI, including setting the number of torsions/rotatable bonds and assigning Gasteiger charges. The screening process was conducted using Oracle Grid Scheduler on a computer cluster running Oracle Sun Grid Engine. The data set of ∼7 million ligands was tested at an exhaustiveness of 5. Exhaustiveness is an AutoDock Vina-specific parameter, which defines the relative amount of thoroughness (in terms of the number of protein−ligand conformations tested) the software uses to evaluate the docking. Protein−ligand binding efficacy was evaluated using the binding affinity energy (kcal/mol) obtained from the final output for each complex and used to identify the top five ligands for further analysis, which included repeat Vina docking at higher exhaustiveness.

Interactions at the Protein−Ligand Complex Interface. Further visualizations of protein−ligand interactions were carried out on the protein−ligand interaction profiler (PLIP) using the protein−ligand complexes generated from the SARS-CoV-2 AutoDock Vina output.[76] PLIP provides information on the number, type, distance, and implicated atoms in interactions such as hydrogen bonding, hydrophobic interactions, π−cation interactions, and π stacking, which occur between the protein and ligand. These were used to further evaluate the energetics of the protein−ligand complex formation and to evaluate the pharmaceutical suitability of the binding cavity as a drug target.

Electrostatic Evaluation of Protein−Ligand Complex. To qualitatively evaluate the contribution of electrostatics to the high binding affinity energies which were obtained, the ESP-DNN neural network was used to generate electrostatic maps (in Coulombs) for the ligands and SARS-CoV-2 Nsp4 protein in their bound conformations as obtained from AutoDock Vina output.[77] Visualization of the electrostatic surface maps enabled the identification of discrete regions of electrostatic complementarity between protein and ligand within the binding cavity.

Molecular Dynamics Methods. Each of the top five protein−ligand complexes was suspended in 150 mM NaCl solutions. The starting points are the complexes generated from the Sars-CoV-2 AutoDock Vina output. The control simulation consisted of the Nsp3Ecto-Nsp4LLL complex. The proteins' topologies were generated using a CHARMM36 force field,[78] while the different therapeutics were described by a CHARMM general force field.[79] The Particle mesh Ewald (PME) method was used for the evaluation of long-range

https://doi.org/10.1021/acsomega.2c06384
ACS Omega 2023, 8, 5349−5360

Coulombic interactions.[80] The time step was set to 1.0 fs. The simulations were performed by NAMD2 in the NPT ensemble (p = 1 bar and T = 300 K), using the Langevin dynamics (γ_{Lang} = 1 ps^{-1}).[81] The trajectories and snapshots were visualized by VMD.[82] The Nonbonding energy between compounds and protein targets was evaluated by NAMD in a generalized Born implicit solvent every 100 frames.[83] The approximate tetrahedral box size was ∼130 Å × 115 Å × 133 Å in neutralized physiological ion buffer 0.15 M NaCl water solution; RMSD and binding energy were calculated for the entire trajectory with a step of 10 frames (Table S3). Each system was pre-equilibrated and minimized for 5 ns before running the molecular dynamics simulations. The last frame was therefore used as a starting point for 200 ns of MD productions. All simulations were performed with backbone constraints for Nsp4LLL supported by Ramachandran plots, which hints that Alphafold simulations reveal a stable structure with unfavorable mutations, Figure S5.

Dendrimer Preparation. The dendrimeric polymer used in this study is the poly(amidoamine) (PAMAM) with six branches for covalent attachment of drugs obtained by the docking simulations.[84] However, the point of attachment between the dendrimer structure and the drugs was crucial: based on the docking position obtained in the previous analyses, an attachment was chosen for each drug to allow the same type of interaction in the binding pocket. Dendrimers were prepared via VMD with Molefacture Plugin, and the initial structure consisted of one attached drug in the same orientation as the molecular docking output. MD simulations were executed for 200 ns with the same conditions as the drug−Nsp4 complexes. A longer simulation for drug 3 dendrimer was performed for 800 ns.

Peptide (β Hairpin) Preparation. Further optimization of the Nsp4 inhibitor was evaluated through the design of a peptide of different sizes by progressively trimming the Nsp3Ecto sequence. In all structures, however, the two β-sheets are kept intact. The smallest peptide was obtained by trimming the amino acid residues 1−9 (Met to Tyr) and residues 33−63 (Ile to Trp) at the ends of the Nsp3Ecto protein sequence. Thus, a β hairpin structure with 23 amino acids (residues 10−32 of Nsp3Ecto) was prepared for simulations. To obtain better stability, a dendrimer structure of PAMAM was used to connect the six β hairpin structures. The N of PAMAM was bonded with C atom of residue 32 (Ser) for each β hairpin. A longer simulation for the peptide alone was performed for 800 ns.

■ ASSOCIATED CONTENT

Supporting Information

The Supporting Information is available free of charge at https://pubs.acs.org/doi/10.1021/acsomega.2c06384.

Supporting figures referenced in the text, including BLASTp results for Nsp3 and Nsp4 for all coronaviruses; comparisons in spike proteins and mutations for SARS-CoV-2; AutoDock Vina maps of complexes; control and simulation data for drugs, peptides and dendrimers; and average binding energy and RMSD for all simulations (PDF)

SARS2_NSP3NSP4_ClusPro3_docked file (PDB)

■ AUTHOR INFORMATION

Corresponding Authors

Amanda M. Acevedo-Jake − *Department of Biomedical Engineering, New Jersey Institute of Technology, Newark, New Jersey 07102, United States*; Email: mauvocado@gmail.com

Petr Král − *Department of Chemistry and Departments of Physics, Pharmaceutical Sciences, and Chemical Engineering, University of Illinois at Chicago, Chicago, Illinois 60607, United States*; orcid.org/0000-0003-2992-9027; Email: pkral@uic.edu

Vivek A. Kumar − *Department of Biological Sciences, Department of Biomedical Engineering, and Department of Chemical and Materials Engineering, New Jersey Institute of Technology, Newark, New Jersey 07102, United States; Department of Endodontics, Rutgers School of Dental Medicine, Newark, New Jersey 07103, United States*; orcid.org/0000-0001-7536-9281; Email: vak@njit.edu

Authors

Abdul-Rahman Azizogli − *Department of Biological Sciences, New Jersey Institute of Technology, Newark, New Jersey 07102, United States*

Varun Pai − *Department of Biological Sciences, New Jersey Institute of Technology, Newark, New Jersey 07102, United States*

Francesco Coppola − *Department of Chemistry, University of Illinois at Chicago, Chicago, Illinois 60607, United States*; orcid.org/0000-0002-2429-204X

Roya Jafari − *Department of Chemistry, University of Illinois at Chicago, Chicago, Illinois 60607, United States*

Joseph B. Dodd-o − *Department of Biomedical Engineering, New Jersey Institute of Technology, Newark, New Jersey 07102, United States*

Rohan Harish − *Department of Electrical and Computer Engineering, New Jersey Institute of Technology, Newark, New Jersey 07102, United States*

Bhavani Balasubramanian − *Department of Chemistry and Environmental Sciences, New Jersey Institute of Technology, Newark, New Jersey 07102, United States*

Jatin Kashyap − *Department of Biomedical Engineering, New Jersey Institute of Technology, Newark, New Jersey 07102, United States*

Complete contact information is available at: https://pubs.acs.org/10.1021/acsomega.2c06384

Author Contributions

◆A.-R.A., V.P., and F.C. contributed equally as co-first authors. A.-R.A., V.P., F.C., R.J., J.B.D., and R.H. carried out the research and made the figures and the manuscript draft. A.M.A.-J., P.K., and V.A.K. provided guidance and oversaw the project. P.K. and V.A.K. obtained funding. All authors wrote and revised manuscript.

Funding

V.A.K. received funding from NIH R15 EY029504, R01DE031812, R01DE029321, R21AR079708, UL1TR003017, NSF IIP 2032392, and the Undergraduate Research and Innovation Program at NJIT.

Notes

The authors declare no competing financial interest.

https://doi.org/10.1021/acsomega.2c06384
ACS Omega 2023, 8, 5349−5360

■ ABBREVIATIONS

Nsps, nonstructural proteins; MD, molecular dynamics; DMVs, double-membrane vesicles; CMs, convoluted membranes; ER, endoplasmic reticulum; ERAD, endoplasmic reticulum-associated degradation; MW, molecular weight; Nsp3, nonstructural protein 3; Nsp3Ecto, nonstructural protein 3 ectodomain; Nsp4, nonstructural protein 4; Nsp4LLL, nonstructural protein 4 large lumenal loop; TM-Score, template modeling score; PLIP, Protein−Ligand Interaction Profiler; CCTOP, constrained consensus TOPology; PME, particle mesh Ewald; PAMAM, poly(amidoamine)

■ REFERENCES

(1) Wu, F.; Zhao, S.; Yu, B.; Chen, Y.-M.; Wang, W.; Song, Z.-G.; Hu, Y.; Tao, Z.-W.; Tian, J.-H.; Pei, Y.-Y.; Yuan, M.-L.; Zhang, Y.-L.; Dai, F.-H.; Liu, Y.; Wang, Q.-M.; Zheng, J.-J.; Xu, L.; Holmes, E. C.; Zhang, Y.-Z. A New Coronavirus Associated with Human Respiratory Disease in China. *Nature* **2020**, *579*, 265−269.

(2) Xu, X.; Chen, P.; Wang, J.; Feng, J.; Zhou, H.; Li, X.; Zhong, W.; Hao, P. Evolution of the Novel Coronavirus from the Ongoing Wuhan Outbreak and Modeling of Its Spike Protein for Risk of Human Transmission. *Sci. China Life Sci.* **2020**, *63*, 457−460.

(3) WHO. Coronavirus Disease (COVID-19) Dashboard, 2022. https://covid19.who.int/.

(4) Chan, J. F.-W.; Kok, K.-H.; Zhu, Z.; Chu, H.; To, K. K.-W.; Yuan, S.; Yuen, K.-Y. Genomic Characterization of the 2019 Novel Human-Pathogenic Coronavirus Isolated from a Patient with Atypical Pneumonia after Visiting Wuhan. *Emerg. Microbes Infect.* **2020**, *9*, 221−236.

(5) Ren, L.-L.; Wang, Y.-M.; Wu, Z.-Q.; Xiang, Z.-C.; Guo, L.; Xu, T.; Jiang, Y.-Z.; Xiong, Y.; Li, Y.-J.; Li, X.-W.; Li, H.; Fan, G.-H.; Gu, X.-Y.; Xiao, Y.; Gao, H.; Xu, J.-Y.; Yang, F.; Wang, X.-M.; Wu, C.; Chen, L.; Liu, Y.-W.; Liu, B.; Yang, J.; Wang, X.-R.; Dong, J.; Li, L.; Huang, C.-L.; Zhao, J.-P.; Hu, Y.; Cheng, Z.-S.; Liu, L.-L.; Qian, Z.-H.; Qin, C.; Jin, Q.; Cao, B.; Wang, J.-W. Identification of a Novel Coronavirus Causing Severe Pneumonia in Human: A Descriptive Study. *Chin. Med. J.* **2020**, *133*, 1015−1024.

(6) SARS-COV-2 variants of concern as of 8 December 2022. https://www.ecdc.europa.eu/en/covid-19/variants-concern (accessed Dec 10, 2022).

(7) Sanyaolu, A.; Okorie, C.; Marinkovic, A.; Haider, N.; Abbasi, A. F.; Jaferi, U.; Prakash, S.; Balendra, V. The Emerging Sars-Cov-2 Variants of Concern. *Ther. Adv. Infect. Dis.* **2021**, *8*, No. 204993612110243.

(8) Khateeb, J.; Li, Y.; Zhang, H. Emerging Sars-Cov-2 Variants of Concern and Potential Intervention Approaches. *Crit. Care* **2021**, *25*, 244.

(9) Wang, Y.; Chen, R.; Hu, F.; Lan, Y.; Yang, Z.; Zhan, C.; Shi, J.; Deng, X.; Jiang, M.; Zhong, S.; Liao, B.; Deng, K.; Tang, J.; Guo, L.; Jiang, M.; Fan, Q.; Li, M.; Liu, J.; Shi, Y.; Deng, X.; Xiao, X.; Kang, M.; Li, Y.; Guan, W.; Li, Y.; Li, S.; Li, F.; Zhong, N.; Tang, X. Transmission, Viral Kinetics and Clinical Characteristics of the Emergent Sars-Cov-2 Delta Voc in Guangzhou, China. *EClinicalMedicine* **2021**, *40*, No. 101129.

(10) Aleem, A.; Samad, A.; Slenker, A. B. *Emerging Variants of Sars-Cov-2 and Novel Therapeutics against Coronavirus (Covid-19)*; StatPearls Publishing LLC: Treasure Island, FL, 2021.

(11) SARS-COV-2 variant classifications and definitions. https://www.cdc.gov/coronavirus/2019-ncov/variants/variant-classifications.html (accessed Dec 10, 2022).

(12) Planas, D.; Veyer, D.; Baidaliuk, A.; Staropoli, I.; Guivel-Benhassine, F.; Rajah, M. M.; Planchais, C.; Porrot, F.; Robillard, N.; Puech, J.; Prot, M.; Gallais, F.; Gantner, P.; Velay, A.; Le Guen, J.; Kassis-Chikhani, N.; Edriss, D.; Belec, L.; Seve, A.; Courtellemont, L.; Péré, H.; Hocqueloux, L.; Fafi-Kremer, S.; Prazuck, T.; Mouquet, H.; Bruel, T.; Simon-Lorière, E.; Rey, F. A.; Schwartz, O. Reduced Sensitivity of Sars-Cov-2 Variant Delta to Antibody Neutralization. *Nature* **2021**, *596*, 276−280.

(13) Herlihy, R.; Bamberg, W.; Burakoff, A.; Alden, N.; Severson, R.; Bush, E.; Kawasaki, B.; Berger, B.; Austin, E.; Shea, M.; Gabrieloff, E.; Matzinger, S.; Burdorf, A.; Nichols, J.; Goode, K.; Cilwick, A.; Stacy, C.; Staples, E.; Stringer, G. Rapid Increase in Circulation of the Sars-Cov-2 B.1.617.2 (Delta) Variant - Mesa County, Colorado, April-June 2021. *MMWR Morb. Mortal Wkly. Rep.* **2021**, *70*, 1084−1087.

(14) Li, B.; Deng, A.; Li, K.; Hu, Y.; Li, Z.; Xiong, Q.; Liu, Z.; Guo, Q.; Zou, L.; Zhang, H.; Zhang, M.; Ouyang, F.; Su, J.; Su, W.; Xu, J.; Lin, H.; Sun, J.; Peng, J.; Jiang, H.; Zhou, P.; Hu, T.; Luo, M.; Zhang, Y.; Zheng, H.; Xiao, J.; Liu, T.; Che, R.; Zeng, H.; Zheng, Z.; Huang, Y.; Yu, J.; Yi, L.; Wu, J.; Chen, J.; Zhong, H.; Deng, X.; Kang, M.; Pybus, O. G.; Hall, M.; Lythgoe, K. A.; Li, Y.; Yuan, J.; He, J.; Lu, J. Viral Infection and Transmission in a Large Well-Traced Outbreak Caused by the Delta Sars-Cov-2 Variant. *Nat. Commun.* **2022**, *13*, No. 460.

(15) Bernal, J. L.; Andrews, N.; Gower, C.; Gallagher, E.; Simmons, R.; Thelwall, S.; Stowe, J.; Tessier, E.; Groves, N.; Dabrera, G.; Myers, R.; Campbell, C. N. J.; Amirthalingam, G.; Edmunds, M.; Zambon, M.; Brown, K. E.; Hopkins, S.; Chand, M.; Ramsay, M. Effectiveness of Covid-19 Vaccines against the B.1.617.2 (Delta) Variant. *N. Engl. J. Med.* **2021**, *385*, 585−594.

(16) Edara, V.-V.; Pinsky, B. A.; Suthar, M. S.; Lai, L.; Davis-Gardner, M. E.; Floyd, K.; Flowers, M. W.; Wrammert, J.; Hussaini, L.; Ciric, C. R.; Bechnak, S.; Stephens, K.; Graham, B. S.; Bayat Mokhtari, E.; Mudvari, P.; Boritz, E.; Creanga, A.; Pegu, A.; Derrien-Colemyn, A.; Henry, A. R.; Gagne, M.; Douek, D. C.; Sahoo, M. K.; Sibai, M.; Solis, D.; Webby, R. J.; Jeevan, T.; Fabrizio, T. P. Infection and Vaccine-Induced Neutralizing-Antibody Responses to the Sars-Cov-2 B.1.617 Variants. *N. Engl. J. Med.* **2021**, *385*, 664−666.

(17) Oostra, M.; te Lintelo, E. G.; Deijs, M.; Verheije, M. H.; Rottier, P. J. M.; de Haan, C. A. M. Localization and Membrane Topology of Coronavirus Nonstructural Protein 4: Involvement of the Early Secretory Pathway in Replication. *J. Virol.* **2007**, *81*, 12323−12336.

(18) Sakai, Y.; Kawachi, K.; Terada, Y.; Omori, H.; Matsuura, Y.; Kamitani, W. Two-Amino Acids Change in the Nsp4 of Sars Coronavirus Abolishes Viral Replication. *Virology* **2017**, *510*, 165−174.

(19) Hagemeijer, M. C.; Ulasli, M.; Vonk, A. M.; Reggiori, F.; Rottier, P. J. M.; de Haan, C. A. M. Mobility and Interactions of Coronavirus Nonstructural Protein 4. *J. Virol.* **2011**, *85*, 4572−4577.

(20) Lei, J.; Kusov, Y.; Hilgenfeld, R. Nsp3 of Coronaviruses: Structures and Functions of a Large Multi-Domain Protein. *Antivir. Res.* **2018**, *149*, 58−74.

(21) Almasy, K. M.; Davies, J. P.; Plate, L. Comparative Host Interactomes of the Sars-Cov-2 Nonstructural Protein 3 and Human Coronavirus Homologs. *Mol. Cell. Proteomics* **2021**, *20*, No. 100120.

(22) Wong, N. A.; Saier, M. H., Jr. The Sars-Coronavirus Infection Cycle: A Survey of Viral Membrane Proteins, Their Functional Interactions and Pathogenesis. *Int. J. Mol. Sci.* **2021**, *22*, 1308.

(23) Asghari, A.; Naseri, M.; Safari, H.; Saboory, E.; Parsamanesh, N. The Novel Insight of Sars-Cov-2 Molecular Biology and Pathogenesis and Therapeutic Options. *DNA Cell Biol.* **2020**, *39*, 1741−1753.

(24) Wolff, G.; Limpens, R. W. A. L.; Zevenhoven-Dobbe, J. C.; Laugks, U.; Zheng, S.; de Jong, A. W. M.; Koning, R. I.; Agard, D. A.; Grünewald, K.; Koster, A. J.; Snijder, E. J.; Bárcena, M. A Molecular Pore Spans the Double Membrane of the Coronavirus Replication Organelle. *Science* **2020**, *369*, 1395−1398.

(25) Fenech, E. J.; Lari, F.; Charles, P. D.; Fischer, R.; Laétitia-Thézénas, M.; Bagola, K.; Paton, A. W.; Paton, J. C.; Gyrd-Hansen, M.; Kessler, B. M.; Christianson, J. C. Interaction Mapping of Endoplasmic Reticulum Ubiquitin Ligases Identifies Modulators of Innate Immune Signalling. *eLife* **2020**, *9*, No. e57306.

(26) Lei, X.; Dong, X.; Ma, R.; Wang, W.; Xiao, X.; Tian, Z.; Wang, C.; Wang, Y.; Li, L.; Ren, L.; Guo, F.; Zhao, Z.; Zhou, Z.; Xiang, Z.;

https://doi.org/10.1021/acsomega.2c06384
ACS Omega 2023, 8, 5349−5360

Wang, J. Activation and Evasion of Type I Interferon Responses by Sars-Cov-2. *Nat. Commun.* **2020**, *11*, No. 3810.
(27) Shi, R.; Feng, Z.; Zhang, X. Integrative Multi-Omics Landscape of Non-Structural Protein 3 of Severe Acute Respiratory Syndrome Coronaviruses. *Genomics Proteomics Bioinform.* **2021**, *19*, 707−726.
(28) van de Leemput, J.; Han, Z. Understanding Individual Sars-Cov-2 Proteins for Targeted Drug Development against Covid-19. *Mol. Cell Biol.* **2021**, *41*, e00185-21.
(29) Olson, E. J.; Brown, D. M.; Chang, T. Z.; Ding, L.; Ng, T. L.; Weiss, H. S.; Koide, Y.; Koch, P.; Rollins, N.; Mach, P.; Meisinger, T.; Bricken, T.; Rollins, J.; Zhang, Y.; Molloy, C.; Zhang, Y.; Queenan, B. N.; Mitchison, T.; Marks, D.; Way, J. C.; Glass, J. I.; Silver, P. A. High-Content Screening of Coronavirus Genes for Innate Immune Suppression Reveals Enhanced Potency of Sars-Cov-2 Proteins, *bioRxiv Preprint* **2021**. DOI: 10.1101/2021.03.02.433434.
(30) Matsuyama, S.; Kawase, M.; Nao, N.; Shirato, K.; Ujike, M.; Kamitani, W.; Shimojima, M.; Fukushi, S. The Inhaled Steroid Ciclesonide Blocks Sars-Cov-2 Rna Replication by Targeting the Viral Replication-Transcription Complex in Cultured Cells. *J Virol.* **2020**, *95*, No. e01648-20.
(31) Covis Pharma Group Announces Top-Line Safety and Efficacy Data from a Phase 3 Placebo-Controlled Covid-19 Study Using Inhaled Corticosteroid (Ciclesonide). Globe Newswire: Zug, Switzerland, 2021.
(32) Lew, W.; Chen, X.; Kim, C. U. Discovery and Development of Gs 4104 (Oseltamivir): An Orally Active Influenza Neuraminidase Inhibitor. *Curr. Med. Chem.* **2000**, *7*, 663−672.
(33) Krohn, A.; Redshaw, S.; Ritchie, J. C.; Graves, B. J.; Hatada, M. H. Novel Binding Mode of Highly Potent Hiv-Proteinase Inhibitors Incorporating the (R)-Hydroxyethylamine Isostere. *J. Med. Chem.* **1991**, *34*, 3340−3342.
(34) Njoroge, F. G.; Chen, K. X.; Shih, N.-Y.; Piwinski, J. J. Challenges in Modern Drug Discovery: A Case Study of Boceprevir, an Hcv Protease Inhibitor for the Treatment of Hepatitis C Virus Infection. *Acc. Chem. Res.* **2008**, *41*, 50−59.
(35) Morris, G. M.; Huey, R.; Lindstrom, W.; Sanner, M. F.; Belew, R. K.; Goodsell, D. S.; Olson, A. J. Autodock4 and Autodocktools4: Automated Docking with Selective Receptor Flexibility. *J. Comput. Chem.* **2009**, *30*, 2785−2791.
(36) Dallakyan, S.; Olson, A. J. Small-Molecule Library Screening by Docking with Pyrx. *Methods Mol. Biol.* **2015**, *1263*, 243−250.
(37) Gligorijević, V.; Renfrew, P. D.; Kosciolek, T.; Leman, J. K.; Berenberg, D.; Vatanen, T.; Chandler, C.; Taylor, B. C.; Fisk, I. M.; Vlamakis, H.; Xavier, R. J.; Knight, R.; Cho, K.; Bonneau, R. Structure-Based Protein Function Prediction Using Graph Convolutional Networks. *Nat. Commun.* **2021**, *12*, No. 3168.
(38) Giulini, M.; Potestio, R. A Deep Learning Approach to the Structural Analysis of Proteins. *Interface Focus* **2019**, *9*, No. 20190003.
(39) Zhang, H.; Shen, Y. Template-Based Prediction of Protein Structure with Deep Learning. *BMC Genomics* **2020**, *21*, 878.
(40) Kuhlman, B.; Bradley, P. Advances in Protein Structure Prediction and Design. *Nat. Rev. Mol. Cell Biol.* **2019**, *20*, 681−697.
(41) Nikolaev, D. M.; Shtyrov, A. A.; Panov, M. S.; Jamal, A.; Chakchir, O. B.; Kochemirovsky, V. A.; Olivucci, M.; Ryazantsev, M. N. A Comparative Study of Modern Homology Modeling Algorithms for Rhodopsin Structure Prediction. *ACS Omega* **2018**, *3*, 7555−7566.
(42) Heo, L.; Feig, M. High-accuracy protein structures by combining machine-learning with physics-based refinement. *Proteins* **2019**, *88* (5), 637−642.
(43) Jumper, J.; Evans, R.; Pritzel, A.; Green, T.; Figurnov, M.; Ronneberger, O.; Tunyasuvunakool, K.; Bates, R.; Žídek, A.; Potapenko, A.; Bridgland, A.; Meyer, C.; Kohl, S. A. A.; Ballard, A. J.; Cowie, A.; Romera-Paredes, B.; Nikolov, S.; Jain, R.; Adler, J.; Back, T.; Petersen, S.; Reiman, D.; Clancy, E.; Zielinski, M.; Steinegger, M.; Pacholska, M.; Berghammer, T.; Bodenstein, S.; Silver, D.; Vinyals, O.; Senior, A. W.; Kavukcuoglu, K.; Kohli, P.; Hassabis, D. Highly Accurate Protein Structure Prediction with Alphafold. *Nature* **2021**, *596*, 583−589.
(44) Tunyasuvunakool, K.; Adler, J.; Wu, Z.; Green, T.; Zielinski, M.; Žídek, A.; Bridgland, A.; Cowie, A.; Meyer, C.; Laydon, A.; Velankar, S.; Kleywegt, G. J.; Bateman, A.; Evans, R.; Pritzel, A.; Figurnov, M.; Ronneberger, O.; Bates, R.; Kohl, S. A. A.; Potapenko, A.; Ballard, A. J.; Romera-Paredes, B.; Nikolov, S.; Jain, R.; Clancy, E.; Reiman, D.; Petersen, S.; Senior, A. W.; Kavukcuoglu, K.; Birney, E.; Kohli, P.; Jumper, J.; Hassabis, D. Highly Accurate Protein Structure Prediction for the Human Proteome. *Nature* **2021**, *596*, 590−596.
(45) AlphaFold. *Alphafold: A Solution to a 50-Year-Old Grand Challenge in Biology*, 2021.
(46) Noble, K. *Artificial Intelligence Solution to a 50-Year-Old Science Challenge Could 'Revolutionise' Medical Research*; CASP, 2020.
(47) Hegedűs, T.; Geisler, M.; Lukács, G. L.; Farkas, B. Ins and Outs of Alphafold2 Transmembrane Protein Structure Predictions. *Cell. Mol. Life Sci.* **2022**, *79*, 73.
(48) Koehler, M. G.; Grigoras, S.; Dunn, W. J., III The Relationship between Chemical Structure and the Logarithm of the Partition Coefficient. *Quant. Struct.−Act. Relat.* **1988**, *7*, 150−159.
(49) Lehmler, H.-J.; Xu, L.; Vyas, S. M.; Ojogun, V. A.; Knutson, B. L.; Ludewig, G. Synthesis, Physicochemical Properties and in Vitro Cytotoxicity of Nicotinic Acid Ester Prodrugs Intended for Pulmonary Delivery Using Perfluorooctyl Bromide as Vehicle. *Int. J. Pharm.* **2008**, *353*, 35−44.
(50) Bailey, M. M.; Berkland, C. J. Nanoparticle Formulations in Pulmonary Drug Delivery. *Med. Res. Rev.* **2009**, *29*, 196−212.
(51) Ziegler, C. G. K.; Allon, S. J.; Nyquist, S. K.; Mbano, I. M.; Miao, V. N.; Tzouanas, C. N.; Cao, Y.; Yousif, A. S.; Bals, J.; Hauser, B. M.; Feldman, J.; Muus, C.; Wadsworth, M. H., II; Kazer, S. W.; Hughes, T. K.; Doran, B.; Gatter, G. J.; Vukovic, M.; Taliaferro, F.; Mead, B. E.; Guo, Z.; Wang, J. P.; Gras, D.; Plaisant, M.; Ansari, M.; Angelidis, I.; Adler, H.; Sucre, J. M. S.; Taylor, C. J.; Lin, B.; Waghray, A.; Mitsialis, V.; Dwyer, D. F.; Buchheit, K. M.; Boyce, J. A.; Barrett, N. A.; Laidlaw, T. M.; Carroll, S. L.; Colonna, L.; Tkachev, V.; Peterson, C. W.; Yu, A.; Zheng, H. B.; Gideon, H. P.; Winchell, C. G.; Lin, P. L.; Bingle, C. D.; Snapper, S. B.; Kropski, J. A.; Theis, F. J.; Schiller, H. B.; Zaragosi, L.-E.; Barbry, P.; Leslie, A.; Kiem, H.-P.; Flynn, J. L.; Fortune, S. M.; Berger, B.; Finberg, R. W.; Kean, L. S.; Garber, M.; Schmidt, A. G.; Lingwood, D.; Shalek, A. K.; Ordovas-Montanes, J.; Banovich, N.; Barbry, P.; Brazma, A.; Desai, T.; Duong, T. E.; Eickelberg, O.; Falk, C.; Farzan, M.; Glass, I.; Haniffa, M.; Horvath, P.; Hung, D.; Kaminski, N.; Krasnow, M.; Kropski, J. A.; Kuhnemund, M.; Lafyatis, R.; Lee, H.; Leroy, S.; Linnarson, S.; Lundeberg, J.; Meyer, K.; Misharin, A.; Nawijn, M.; Nikolic, M. Z.; Ordovas-Montanes, J.; Pe'er, D.; Powell, J.; Quake, S.; Rajagopal, J.; Tata, P. R.; Rawlins, E. L.; Regev, A.; Reyfman, P. A.; Rojas, M.; Rosen, O.; Saeb-Parsy, K.; Samakovlis, C.; Schiller, H.; Schultze, J. L.; Seibold, M. A.; Shalek, A. K.; Shepherd, D.; Spence, J.; Spira, A.; Sun, X.; Teichmann, S.; Theis, F.; Tsankov, A.; van den Berge, M.; von Papen, M.; Whitsett, J.; Xavier, R.; Xu, Y.; Zaragosi, L.-E.; Zhang, K. Sars-Cov-2 Receptor Ace2 Is an Interferon-Stimulated Gene in Human Airway Epithelial Cells and Is Detected in Specific Cell Subsets across Tissues. *Cell* **2020**, *181*, 1016−1035.
(52) Muegge, I. Selection Criteria for Drug-Like Compounds. *Med. Res. Rev.* **2003**, *23*, 302−321.
(53) Xu, J.; Stevenson, J. Drug-Like Index: A New Approach to Measure Drug-Like Compounds and Their Diversity. *J. Chem. Inf. Comput. Sci.* **2000**, *40*, 1177−1187.
(54) Frimurer, T. M.; Bywater, R.; Naerum, L.; Lauritsen, L. N.; Brunak, S. Improving the Odds in Discriminating "Drug-Like" from "Non Drug-Like" Compounds. *J. Chem. Inf. Comput. Sci.* **2000**, *40*, 1315−1324.
(55) Lipinski, C. A.; Lombardo, F.; Dominy, B. W.; Feeney, P. J. Experimental and Computational Approaches to Estimate Solubility and Permeability in Drug Discovery and Development Settings. *Adv. Drug Delivery Rev.* **2001**, *46*, 3−26.
(56) Sen, S.; Han, Y.; Rehak, P.; Vukovic, L.; Kral, P. Computational Studies of Micellar and Nanoparticle Nanomedicines. *Chem. Soc. Rev.* **2018**, *47*, 3849−3860.

https://doi.org/10.1021/acsomega.2c06384
ACS Omega 2023, 8, 5349−5360

(57) Lan, J.; Ge, J.; Yu, J.; Shan, S.; Zhou, H.; Fan, S.; Zhang, Q.; Shi, X.; Wang, Q.; Zhang, L.; Wang, X. Structure of the Sars-Cov-2 Spike Receptor-Binding Domain Bound to the Ace2 Receptor. *Nature* **2020**, *581*, 215−220.
(58) Lei, J.; Zhou, Y.; Xie, D.; Zhang, Y. Mechanistic Insights into a Classic Wonder Drug—Aspirin. *J. Am. Chem. Soc.* **2015**, *137*, 70−73.
(59) Lin, Y.-L.; Roux, B. Computational Analysis of the Binding Specificity of Gleevec to Abl, C-Kit, Lck, and C-Src Tyrosine Kinases. *J. Am. Chem. Soc.* **2013**, *135*, 14741−14753.
(60) Cournia, Z.; Allen, B.; Sherman, W. Relative Binding Free Energy Calculations in Drug Discovery: Recent Advances and Practical Considerations. *J. Chem. Inf. Model.* **2017**, *57*, 2911−2937.
(61) Chand, G. B.; Banerjee, A.; Azad, G. K. Identification of Twenty-Five Mutations in Surface Glycoprotein (Spike) of Sars-Cov-2 among Indian Isolates and Their Impact on Protein Dynamics. *Gene Rep.* **2020**, *21*, No. 100891.
(62) Lo Presti, A.; Rezza, G.; Stefanelli, P. Selective Pressure on Sars-Cov-2 Protein Coding Genes and Glycosylation Site Prediction. *Heliyon* **2020**, *6*, e05001.
(63) O'Donoghue, S. I.; Schafferhans, A.; Sikta, N.; Stolte, C.; Kaur, S.; Ho, B. K.; Anderson, S.; Procter, J. B.; Dallago, C.; Bordin, N.; Adcock, M.; Rost, B. Sars-Cov-2 Structural Coverage Map Reveals Viral Protein Assembly, Mimicry, and Hijacking Mechanisms. *Mol. Syst. Biol.* **2021**, *17*, No. e10079.
(64) Gorkhali, R.; Koirala, P.; Rijal, S.; Mainali, A.; Baral, A.; Bhattarai, H. K. Structure and Function of Major Sars-Cov-2 and Sars-Cov Proteins. *Bioinform. Biol. Insights* **2021**, *15*, No. 117793222110258.
(65) Stigliani, M.; Haghi, M.; Russo, P.; Young, P. M.; Traini, D. Antibiotic Transport across Bronchial Epithelial Cells: Effects of Molecular Weight, Logp and Apparent Permeability. *Eur. J. Pharm. Sci.* **2016**, *83*, 45−51.
(66) Cheraghi, M.; Negahdari, B.; Daraee, H.; Eatemadi, A. Heart Targeted Nanoliposomal/Nanoparticles Drug Delivery: An Updated Review. *Biomed. Pharmacother.* **2017**, *86*, 316−323.
(67) Altschul, S. F.; Gish, W.; Miller, W.; Myers, E. W.; Lipman, D. J. Basic Local Alignment Search Tool. *J. Mol. Biol.* **1990**, *215*, 403−410.
(68) Jumper, J.; Hassabis, D.; Tunyasuvunakool, K. Computational predictions of protein structures associated with covid-19. https://www.deepmind.com/open-source/computational-predictions-of-protein-structures-associated-with-covid-19 (accessed Dec 10, 2022).
(69) Moelbert, S.; Emberly, E.; Tang, C. Correlation between Sequence Hydrophobicity and Surface-Exposure Pattern of Database Proteins. *Protein Sci.* **2004**, *13*, 752−762.
(70) Dobson, L.; Reményi, I.; Tusnády, G. E. Cctop: A Consensus Constrained Topology Prediction Web Server. *Nucleic Acids Res.* **2015**, *43*, W408−W412.
(71) Kozakov, D.; Hall, D. R.; Xia, B.; Porter, K. A.; Padhorny, D.; Yueh, C.; Beglov, D.; Vajda, S. The Cluspro Web Server for Protein−Protein Docking. *Nat. Protoc.* **2017**, *12*, 255−278.
(72) Wood, C. W.; Ibarra, A. A.; Bartlett, G. J.; Wilson, A. J.; Woolfson, D. N.; Sessions, R. B. Balas: Fast, Interactive and Accessible Computational Alanine-Scanning Using Budealascan. *Bioinformatics* **2020**, *36*, 2917−2919.
(73) Sterling, T.; Irwin, J. J. Zinc 15 − Ligand Discovery for Everyone. *J. Chem. Inf. Model.* **2015**, *55*, 2324−2337.
(74) O'Boyle, N. M.; Banck, M.; James, C. A.; Morley, C.; Vandermeersch, T.; Hutchison, G. R. Open Babel: An Open Chemical Toolbox. *J. Cheminf.* **2011**, *3*, 33.
(75) Trott, O.; Olson, A. J. Autodock Vina: Improving the Speed and Accuracy of Docking with a New Scoring Function, Efficient Optimization, and Multithreading. *J. Comput. Chem.* **2010**, *31*, 455−461.
(76) Salentin, S.; Schreiber, S.; Haupt, V. J.; Adasme, M. F.; Schroeder, M. Plip: Fully Automated Protein−Ligand Interaction Profiler. *Nucleic Acids Res.* **2015**, *43*, W443−W447.
(77) Rathi, P. C.; Ludlow, R. F.; Verdonk, M. L. Practical High-Quality Electrostatic Potential Surfaces for Drug Discovery Using a Graph-Convolutional Deep Neural Network. *J. Med. Chem.* **2020**, *63*, 8778−8790.
(78) Lee, J.; Cheng, X.; Swails, J. M.; Yeom, M. S.; Eastman, P. K.; Lemkul, J. A.; Wei, S.; Buckner, J.; Jeong, J. C.; Qi, Y.; Jo, S.; Pande, V. S.; Case, D. A.; Brooks, C. L., 3rd; MacKerell, A. D., Jr.; Klauda, J. B.; Im, W. Charmm-Gui Input Generator for Namd, Gromacs, Amber, Openmm, and Charmm/Openmm Simulations Using the Charmm36 Additive Force Field. *J. Chem. Theory Comput.* **2016**, *12*, 405−413.
(79) Vanommeslaeghe, K.; Hatcher, E.; Acharya, C.; Kundu, S.; Zhong, S.; Shim, J.; Darian, E.; Guvench, O.; Lopes, P.; Vorobyov, I.; Mackerell, A. D., Jr. Charmm General Force Field: A Force Field for Drug-Like Molecules Compatible with the Charmm All-Atom Additive Biological Force Fields. *J. Comput. Chem.* **2010**, *31*, 671−690.
(80) Darden, T.; York, D.; Pedersen, L. Particle Mesh Ewald: An N·Log (N) Method for Ewald Sums in Large Systems. *J. Chem. Phys.* **1993**, *98*, 10089−10092.
(81) Phillips, J. C.; Hardy, D. J.; Maia, J. D.; Stone, J. E.; Ribeiro, J. V.; Bernardi, R. C.; Buch, R.; Fiorin, G.; Hénin, J.; Jiang, W.; et al. Scalable Molecular Dynamics on Cpu and Gpu Architectures with Namd. *J. Chem. Phys.* **2020**, *153*, No. 044130.
(82) Humphrey, W.; Dalke, A.; Schulten, K. Vmd: Visual Molecular Dynamics. *J. Mol. Graphics* **1996**, *14*, 33−38.
(83) Tanner, D. E.; Chan, K.-Y.; Phillips, J. C.; Schulten, K. Parallel Generalized Born Implicit Solvent Calculations with Namd. *J. Chem. Theory Comput.* **2011**, *7*, 3635−3642.
(84) Esfand, R.; Tomalia, D. A. Poly(Amidoamine) (Pamam) Dendrimers: From Biomimicry to Drug Delivery and Biomedical Applications. *Drug Discovery Today* **2001**, *6*, 427−436.

https://doi.org/10.1021/acsomega.2c06384
ACS Omega 2023, 8, 5349−5360